PROCEEDINGS OF SCIENCE

Modelling Variability in the Emission and Polarization of Sub-Parsec Scale AGN Jets with 3D RMHD PLUTO Simulations

Izak van der Westhuizen,[a,*] **Reuben Immelman,**[a] **Brian van Soelen**[a] **and Bhargav Vaidya**[b]

[a] *University of the Free State, Bloemfontein, South Africa*
[b] *Indian Institute of Technology Indore, Indore, India*

E-mail: vanderwesthuizenip@ufs.ac.za

Radio-loud active galactic nuclei (RLAGN) emit radiation across most of the electromagnetic spectrum. The lower-energy component (Radio - Soft X-rays) is typically dominated by synchrotron emission from non-thermal electrons in a relativistic jet. RLAGN are known to be highly variable on both short (intra-day) and long (months to years) timescales. Most of the variability observed in the optical and higher-energy regimes has been associated with sub-parsec to parsec scale emission regions located within the jet. In this study, we investigate the link between observations and the kinematics of the sub-parsec-scale relativistic jet using 3D relativistic magnetohydrodynamic (RMHD) simulations. The simulations employ a two-component jet model, consisting of a fast spine ($\Gamma = 10$) and a slower sheath ($\Gamma = 3$). The jet model features an initial helical magnetic field with a magnitude of 50 mG in the spine and 5 mG in the sheath. In order to simulate variability in the jet, a density perturbation is introduced at the jet inlet and allowed to evolve with time. The simulations are carried out using a modified version of the PLUTO code, which includes the injection of Lagrangian tracer particles, representing the non-thermal electron distribution, used to model the synchrotron emission. The spectral energy distribution of these particles are evolved over time to include effects from diffusive shock acceleration and radiative cooling. This is used to calculate the I, Q, and U Stokes parameters, for arbitrary lines of sight, accounting for relativistic transformations and light travel time. The Stokes parameters are used to reproduce simulated light curves of the flux, polarization degree and polarization angle.

High Energy Astrophysics in Southern Africa (HEASA2025)
16-20 September, 2025
University of Johannesburg, South Africa

*Speaker

 ISSN 1824-8039 . Published by SISSA Medialab.

PoS(HEASA2025)026

1. Introduction

Radio-loud Active Galactic Nuclei (AGN) produce powerful jets that dominate their emission. They exhibit a wide variety of observational features and are sub-divided into a range of different classes. The observed differences between these classes originate either from intrinsic differences in their structure or from the observation angle. The morphology and dynamics of their relativistic jets can be investigated through RMHD simulations [see e.g. 1, 2]. Radio-loud Active Galactic Nuclei are known for their variability, showing both long-term and short-term variability, with blazar having been observed down to minute timescales [3]. The emission from blazars has often been modelled by a single dominant emission zone. This emission zone can originate from a strong shock within the jet that accelerates non-thermal electrons [4]. Recently, the IXPE observatory has been able to measure the X-ray polarization of blazars, which has opened an additional avenue to constrain the emission regions of these sources. These observations typically show an increase in polarization towards higher energies, which is consistent with a shock in jet model [5]. The aim of this work is to model the emission from recollimation shocks in a parsec-scale jet using 3D RMHD simulations.

2. Numerical simulations

In order to simulate the dynamics and morphology of a parsec-scale section of a relativistic jet the opensource PLUTO code was used [6]. For our model the RMHD physics module was used along with RK2 time stepping, linear spatial interpolation and the HLL Riemann solver. The choice of solvers were based on previous tests that have been done using the Lagrangian particle module. The domain consisted of a Cartesian grid with $100 \times 100 \times 600$ cells representing a region of $10 \times 10 \times 60$ pc.

The jet was defined as a cylindrical section in the centre of the domain. A two component jet model was considered with a fast moving spine ($\Gamma = 10$) and a slower moving sheath ($\Gamma = 3$). The radius of the inner spine was set to 0.33 pc and the outer sheath was set to 1.0 pc. An underdense jet was considered with the ratio of jet to ambient density (η) selected as 10^{-3} for the spine and 10^{-2} for the sheath. An over pressured jet model was considered in order to create a recollimation shock. Finally a helical magnetic field was set-up following the model discussed by [7] [see also 8], with the toroidal component given by,

$$B_\phi = \begin{cases} B_{\text{spine}} \left(\frac{R}{R_{\text{spine}}}\right)^{\alpha_{\text{spine}}/2}; & \text{if } 0 \le R < R_{\text{spine}} \\ B_{\text{sheath}} \left(\frac{R}{R_{\text{spine}}}\right)^{\alpha_{\text{sheath}}/2}; & \text{if } R_{\text{spine}} \le R \le R_{\text{sheath}} \\ 0; & \text{if } R > R_{\text{sheath}} \end{cases} \tag{1}$$

where R_{spine} and R_{sheath} are the radii of the spine and sheath, respectively, and B_{spine} and B_{sheath} are the magnetic field parameters of the spine and the sheath. The magnetic field exponent, α, was set to 0.5 for the spine and -2.0 for the sheath. Due to different choices for B_{spine} and B_{sheath}, a discontinuity arises at the interface of the sheath and the spine. To ensure a seamless transition between the two profiles, a hyperbolic tangential smoothing function was applied at the intersections.

Table 1: Summary of simulation parameters

Parameter:	**Spine:**	**Sheath:**
Lorentz factor (Γ)	10	3
Jet Radius (R)	0.33 pc	1.0 pc
Density ratio (η_ρ)	10^{-3}	10^{-2}
Pressure ratio (η_p)	4.0	2.0
Magnetic field (B)	50 mG	5 mG
Pitch profile parameter (α)	0.5	−2.0

The z component of the magnetic field was set equal to the toriodal components in order to obtain a constant pitch angle. The jet parameters are summarised in Table 1.

In order to investigate the effect of a variable component propagating through the jet, a denser blob of material ($\eta_\rho = 1$) was injected at the base of the jet after a quasi-equilibrium state was obtained. The blob consisted of a cylindrical region with radius $R_{\rm blob} = 0.5R_{\rm spine}$ and length 0.3 pc, resulting in a light crossing time of ≈ 1 yr. The magnetic field strength of the blob was also increased by a factor 10.

3. Synchrotron emission

The synchrotron emission was modelled from the simulation using a modified version of the Lagrangian particle module in PLUTO [9]. Each Lagrangian particle was assigned a discrete energy distribution in the form of a single power-law,

$$n(\gamma) = n_0 \gamma^{-p}, \tag{2}$$

where n_0 is a normalization factor, γ is the electron energy and p is the spectral index. For the initial injected distribution, a steep power-law index was chosen with $p = 5$ while minimum and maximum energies of $\gamma_{min} = 10^2$ and $\gamma_{max} = 10^7$ were used. The electron distribution was evolved as it moved through the simulation, subject to diffuse shock acceleration and synchrotron cooling.

The synchrotron emission and absorption coefficients were calculated based on the energy spectrum of each cell. The polarized and unpolarized emission coefficients are given by [10],

$$j'_I(\nu', \hat{\mathbf{n}}'_{\mathbf{los}}) = \frac{\sqrt{3}}{4\pi} \frac{q^3}{m_e c^2} |\mathbf{b} \times \hat{\mathbf{n}}'_{\mathbf{los}}| \int n'_e(\gamma') F(x)\, \mathrm{d}\gamma', \tag{3}$$

$$j'_{pol}(\nu', \hat{\mathbf{n}}'_{\mathbf{los}}) = \frac{\sqrt{3}}{2\pi} \frac{q^3}{m_e c^2} |\mathbf{b} \times \hat{\mathbf{n}}'_{\mathbf{los}}| \int n'_e(\gamma') G(x)\, \mathrm{d}\gamma'. \tag{4}$$

where q and m_e are the fundamental charge and mass of an electron, respectively, c is the speed of light, $\mathbf{b}$ is the magnetic field in the co-moving frame, and $\hat{\mathbf{n}}_{\mathbf{los}}$ is the line of sight vector. The Stokes components can be calculated by,

$$\begin{aligned} j_Q &= j_{\rm pol} \cos 2\chi \\ j_U &= j_{\rm pol} \sin 2\chi, \end{aligned} \tag{5}$$

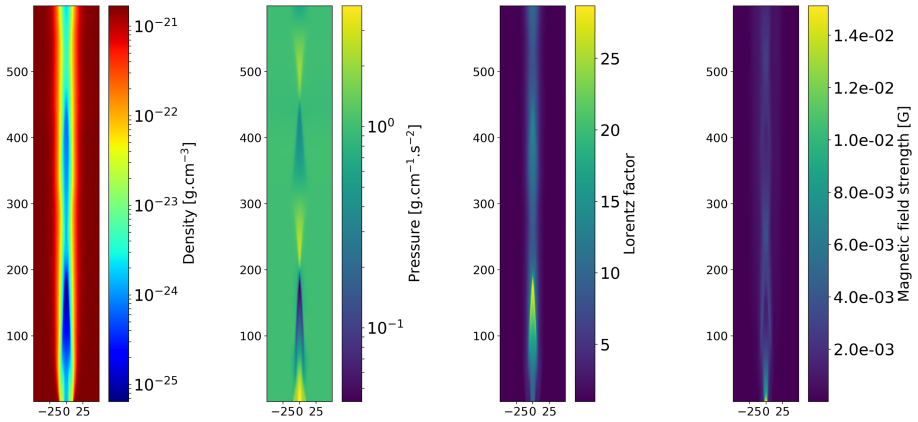

Figure 1: Two-dimensional slices of the xz-plane showing different properties of the simulation. The spatial axes are given in terms of cell number. Each cell corresponds to 0.1 pc.

where the polarization angle χ is defined in terms of the plane orthogonal to the line of sight [9].

Similarly, the absorption coefficients can be given by,

$$\alpha'_{\rm pol}(\nu', \hat{\mathbf{n}}'_{\rm los}) = -\frac{\sqrt{3}}{8\pi}\frac{q^3}{m_e^2 c^2 \nu^2}|\mathbf{b}\times\hat{\mathbf{n}}'_{\rm los}|\int G(x)\gamma^2\frac{\partial}{\partial\gamma}\left[\frac{n'_e(\gamma')}{\gamma^2}\right]\mathrm{d}\gamma'\mathrm{d}\Omega'_\tau. \tag{6}$$

$$\alpha'_I(\nu', \hat{\mathbf{n}}'_{\rm los}) = -\frac{\sqrt{3}}{8\pi}\frac{q^3}{m_e^2 c^2 \nu^2}|\mathbf{b}\times\hat{\mathbf{n}}'_{\rm los}|\int \gamma^2\frac{\partial}{\partial\gamma}\left[\frac{n'_e(\gamma')}{\gamma^2}\right]F(x)\,\mathrm{d}\gamma'\mathrm{d}\Omega'_\tau. \tag{7}$$

The primed quantities represent variables in the co-moving frame of the fluid.

To calculate the I, Q, and U Stokes parameters, we integrate the emission coefficients along the line of sight $\hat{\mathbf{n}}_{\rm los}$ [11] with,

$$\frac{d}{ds}\begin{bmatrix} I \\ Q \\ U \end{bmatrix} = \begin{bmatrix} j_I \\ j_Q \\ j_U \end{bmatrix} - \begin{bmatrix} \alpha_I & \alpha_Q & \alpha_U \\ \alpha_Q & \alpha_I & 0 \\ \alpha_U & 0 & \alpha_I \end{bmatrix}\begin{bmatrix} I \\ Q \\ U \end{bmatrix}. \tag{8}$$

Both relativistic transformations and light travel time effects are taken into account for the integration.

4. Results

The RMHD simulation was evolved until a quasi-steady state was achieved. The resulting structure of the simulation is shown in figure 1. The beam of the jet in the simulation remains stable throughout the length of the domain. The jet radius changes along the jet axis due to the initial pressure imbalance. This causes the density, pressure, Lorentz factor, and magnetic field strength to vary along the z-axis. The formation of two recollimation shocks can be observed in the pressure plot.

Figure 2 shows intensity maps that were calculated for the equilibrium state at different frequencies for an inclination angle of $\theta = 30°$ relative to the jet axis. At radio ($\nu = 10^9$ Hz) frequencies,

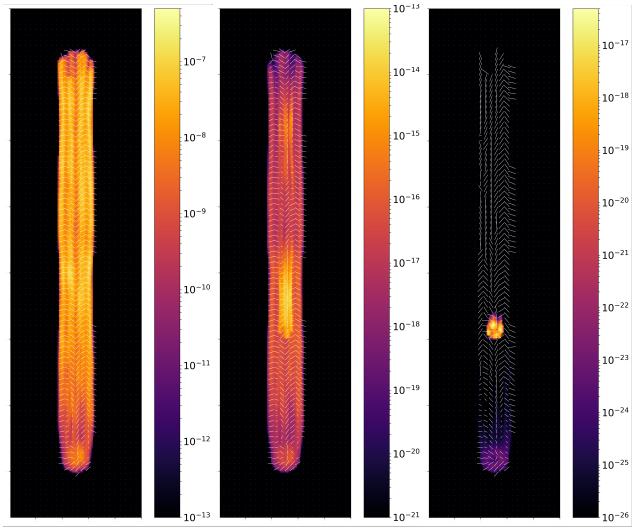

Figure 2: Integrated intensity maps calculated for an observation angle of $\theta = 30°$ at (*left*) radio ($\nu = 10^9$ Hz), (*middle*) optical ($\nu = 10^{14}$ Hz), and (*right*) X-ray ($\nu = 10^{17}$ Hz) frequencies. The colour scale is given in log scaling with units of erg.s^{-1}.cm^{-2}.sr^{-1}.Hz^{-1}. The polarization vectors are over plotted as white bars.

the sheath region dominates the emission, resulting in a mostly uniform appearance along its axis. The recollimation shocks that form in the spine of the jet are not visible at these lower frequencies. In the radio regime, the emission is produced by lower-energy electrons that are dominant in the steep initial electron spectrum, which results in a bright radio jet. The effects of radiative cooling for these lower energy electrons are small across the length of the domain, which produces the uniform appearance along the beam of the jet.

There are two main factors contributing to the absence of the recollimation shocks at lower frequencies. First is the effect of Doppler boosting between the two components of the jet. At this angle, the emission in the faster moving spine is deboosted ($\delta_{spine} = 0.72$) relative to the slower moving sheath ($\delta_{spine} = 1.8$). Secondly, there is an increase in self-absorption at lower frequencies, with the optical depth ($\tau = \alpha ds$) reaching a maximum $\tau_{9\mathrm{GHz}} = 4.2$ for certain cells in the sheath. This results in an opaque sheath at these frequencies.

For emission at optical ($\nu = 10^{14}$ Hz) and X-ray ($\nu = 10^{17}$ Hz) frequencies, the extended jet becomes fainter, and the recollimation shock in the spine dominates the emission. The recollimation shocks are locations at which particle acceleration occurs, resulting in a flatter electron spectrum with a higher maximum energy. This results in brighter emission at higher frequencies. The size of the emission region decreases as the frequency increases due to faster synchrotron cooling for higher energy electrons. The self-absorption at these energies is negligible, and the jet is optically thin.

The variable blob component was injected, and intensity maps were calculated at different frequencies and observation angles. Figure 3 shows the light curve (in computation time steps) calculated for the observation angles $\theta = 2°$ (left) and $\theta = 30°$ (right) at optical and X-ray frequencies. At both optical and X-rays frequencies, the peak flux occurs after the blob has propagated through the recollimation shock. For both observation angles, the optical emission

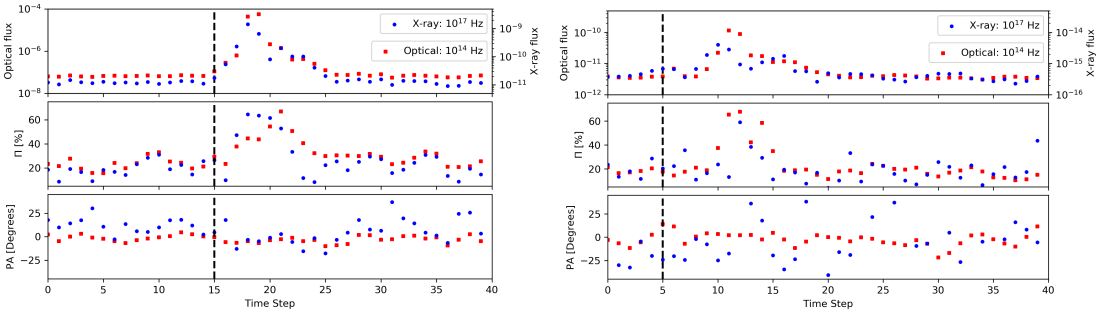

Figure 3: Synthetic light curves from the injection of an overdense blob for inclination angles of (left) $\theta = 2°$ and (right) $\theta = 30°$. The top panel shows the relative change in flux in arbitrary units. The middle panel shows the linear polarization degree, and the lower panel shows the polarization angle relative to the projected jet axis. The blue points represent X-ray frequencies ($\nu = 10^{17}$ Hz) and the red points represent optical frequencies ($\nu = 10^{14}$ Hz). The black dashed lines designate the timestep that the blob was injected. Each time step represents 120 days in the observer frame.

peaks a timestep after the X-ray emission. This happens because the optical component remains brighter for longer, allowing it to fill a larger volume of the jet.

At both optical and X-ray frequencies, the initial degree of polarization is $\approx 20\%$. The degree of polarization increases with the injection of the blob, with the increase in the optical polarization lagging behind the flux. The simulations give a maximum degree of polarization $> 60\%$, close to the theoretical maximum, and higher than is measured in observations. This is because the simulations have a perfectly ordered helical magnetic field. The polarization angle shows some variations, however, no correlation can be seen between the polarization angle and the change in flux. The polarization angle a the X-ray frequency is significantly more variable than at the optical frequency, however, this is a numerical effect due to the lower X-ray flux.

5. Conclusion

RMHD simulations of parsec-scale jets were used to model the synchrontron emission of AGN jets. The emission originates from the extended jet for lower energies, however, as the energy of the emission increases, it is limited to regions of particle acceleration at the position of recollimation shocks.

Variable flux and polarization was reproduced by injecting a density blob into the jet. The peak emission in optical and X-ray corresponded to the blob crossing the recollimation shock, accompanied by an increase in the degree of polarization. The polarization level is higher than typically observed in AGN due to the initial set-up of a perfectly ordered helical magnetic field. Future improvements for the study includes modelling synthetic SED's, placing better constraints on the initial non-thermal spectrum and considering additional forms of variability (for example a precessing jet model).

References

[1] Komissarov S., Porth O., 2021, NewAR, 92, 101610. doi:10.1016/j.newar.2021.101610

[2] Martí J.-M., 2019, Galaxy, 7, 24. doi:10.3390/galaxies7010024

[3] Aharonian F., Akhperjanian A. G., Anton G., Barres de Almeida U., Bazer-Bachi A. R., Becherini Y., Behera B., et al., 2009, A&A, 502, 749. doi:10.1051/0004-6361/200912128

[4] Marscher A. P., 2014, ApJ, 780, 87. doi:10.1088/0004-637X/780/1/87

[5] Kouch P. M., Liodakis I., Middei R., Kim D. E., Tavecchio F., Marscher A. P., Marshall H. L., et al., 2024, A&A, 689, A119. doi:10.1051/0004-6361/202449166

[6] Mignone A., Bodo G., Massaglia S., Matsakos T., Tesileanu O., Zanni C., Ferrari A., 2007, ApJS, 170, 228. doi:10.1086/513316

[7] Meliani Z., Keppens R., 2009, ApJ, 705, 1594. doi:10.1088/0004-637X/705/2/1594

[8] Fichet de Clairfontaine G., Meliani Z., Zech A., Hervet O., 2021, A&A, 647, A77. doi:10.1051/0004-6361/202039654

[9] Vaidya B., Mignone A., Bodo G., Rossi P., Massaglia S., 2018, ApJ, 865, 144. doi:10.3847/1538-4357/aadd17

[10] Rybicki G. B., Lightman A. P., Radiative Processes in Astrophysics, 1979, John Wiley & Sons, Ltd, doi:https://doi.org/10.1002/9783527618170

[11] Galishnikova A., Philippov A., Quataert E., 2023, ApJ, 957, 103. doi:10.3847/1538-4357/acfa77